Check for updates

Polyoxometalate-based materials: quasi-homogeneous single-atom catalysts with atomic-precision structures

Shiqing He, Qingda Liu [ID] * and Xun Wang [ID] *

Polyoxometalates (POMs) are early-transition-metal oxide clusters with diverse structures and extensive functionality. Due to their excellent redox properties and stability, POM clusters can serve as ligands and supports for constructing single-atom catalysts (SACs) with atomic-precision structures, where the coordination states and loading of active sites can be controlled precisely. Metal-substituted POM clusters are also promising candidates to act as sub-nanometer building blocks, where neoteric morphologies and enhanced catalytic properties have been obtained using these cluster-based assemblies. Moreover, POM-based single-atom catalysts display the advantages of both heterogeneous and homogeneous catalysts, in addition to excellent solubility and reusability. This perspective summarizes recent progress relating to polyoxometalate-based single-atom catalysts, including the synthesis and applications of metal-substituted POM clusters and the use of cluster-based assemblies as single-atom catalysts. Future research directions and challenges are also expounded upon, and this work may allow a comprehensive understanding of and novel insights into cluster-based single-atom catalysts.

1. Introduction

Single-atom catalysts (SACs) have gained a surge of interest since their emergence,[1–5] which is due to their unprecedented catalytic activities in a wide range of applications.[6–13] The atomically dispersed metal active sites of SACs dramatically enlarge the effective contact area during reactions, also allowing the possibility of the precise control of the coordination state and electronic structure of single-atom sites. The typical preparation of SACs involves anchoring metal ions on various supports, including metal oxides, MOFs, ZIFs, COFs, and other carbon-based materials.[14–19] Although the development of SACs has been fast-tracked, there are still challenges ahead. The characterization of single-atom sites is extremely difficult without the utilization of extended X-ray absorption fine structure (EXAFS) spectroscopy and spherical aberration electron microscopy with atomic resolution, and the actual coordination states of metal atoms cannot commonly be accurately described. Compared with the bonding between atoms inside supports, interactions between single-atom sites and supports are relatively weak, which may lead to the gradual dissociation of single-atom sites during catalytic reactions. Thus, the high

Key Lab of Organic Optoelectronics and Molecular Engineering, Department of Chemistry, Tsinghua University, Beijing 100084, China. E-mail: wangxun@mail.tsinghua.edu.cn; liuqingda@mail.tsinghua.edu.cn

Shiqing He received her bachelor's degree in chemistry from the Department of Chemistry, Tsinghua University in 2021. She is currently a PhD candidate at Tsinghua University. Her current research interests focus on nanomaterials.

Qingda Liu received his bachelor's and PhD degrees in chemistry from the Department of Chemistry, Tsinghua University in 2016 and 2021, respectively. He is currently a post-doctoral researcher at Tsinghua University. His current research focuses on the synthesis and application of polyoxometalate-based nanostructures.

5758 | *J. Mater. Chem. A*, 2022, **10**, 5758–5770

This journal is © The Royal Society of Chemistry 2022

loading of active sites (>1%) and good SAC catalytic stability cannot be achieved concurrently. In light of this, easily feasible approaches and well-defined system models are crucial for the design and synthesis of novel SACs with controllable and predictable properties.

Polyoxometalates (POMs) are atomic-precision clusters with a variety of structures and compositions, and they have diverse functions in photochemistry, catalysis, electronics, electro-chemistry, medicine, *etc.*[20–26] The surface of a POM cluster is covered with oxygen, which is an ideal support for atomically dispersed metals. Due to the rich-substitutional chemistry of POM clusters, metal active sites can be inserted into the structures *via* substitution or adsorption, covalently or non-covalently, with precisely controlled coordination states and loading amounts.[27–29] Simple characterization techniques, including crystal X-ray diffraction (XRD), nuclear magnetic resonance (NMR) spectroscopy, infrared spectroscopy (IR), and mass spectroscopy (MS) are commonly used to reveal the exact structures of cluster-based SACs. Moreover, the electronic structure of a POM cluster is close to a "superatom", which can be tuned precisely at the atomic level.[30,31] Owing to the electron-rich properties, POM clusters are able to accept or lose several electrons without structural change during redox reactions. Therefore, the POM supports may serve as electron buffers in POM-based SACs, where the electronic structure of metal active sites and the overall catalytic performances of SACs can be controlled precisely. Other than acting as conventional supports, POM units display excellent solubility at the sub-nanometer scale in many solvents, and they can act as homogeneous catalysts for reactions. Upon the addition of poor solvents, POM-based catalysts can be collected and recycled without structural change. Considering the existence of the advantages of both heterogeneous and homogeneous catalysts, POM-based SACs can also be regarded as quasi-homogeneous catalysts.

In this paper, we will summarize recent progress relating to POM-based SACs with well-defined structures and diverse functionalities, including isolated POM clusters, POM-based assemblies, and supported POM structures. Perspectives and challenges relating to POM-based SACs are also discussed. Research into POM-based SACs is just getting off the ground,

and more effort is needed to explore cluster-based structures. We hope that this perspective may provide novel insight into the design and synthesis of SACs.

2. Interactions between single atoms and POM supports

Before discussing the applications and properties of POM-based SACs, the interactions between single atoms and POM clusters will be briefly introduced. The loading of metal active sites proceeds typically in two ways. (1) Substitution. Normally, through mixing POM clusters and metal salts in aqueous solution at a certain pH and temperature, metal-substituted POM clusters can be prepared containing covalently connected metal sites with well-defined structures and locations. Single-atom sites are supported by lacunary POM anions with high negative charge. (2) Absorption. Plenary POM clusters, such as $[PW_{12}O_{40}]^{3-}$ and $[PMo_{12}O_{40}]^{3-}$, are commonly used as supports. Metal ions are generally absorbed on surface oxygen atoms of the POM cluster with a low coordination number. POM SACs prepared *via* this approach display lower charge, with a tunable amount of metal loading but lower catalytic stability. In both cases, the metal sites are fully exposed and coordinated in an unsaturated manner; they can serve as binding sites during catalytic reactions.

Generally, positively charged metal ions spontaneously attach to the surfaces of negatively charged POM clusters. Interactions between metal atoms and POM supports involve covalent bonds (or coordination bonds) and electrostatic attraction, giving higher-stability single-atom sites compared with electroneutral supports. For the loading of metal active sites *via* substitution, the chelate coordination environment further improves the stability of POM-based SACs. Isolated POM SACs exhibit excellent stability in both aqueous and organic systems. For example, the structure of $K_{10}[Co(H_2O)_2(SiW_{10}O_{35})_2]$ can be maintained after photocatalytic water oxidation with no decomposed Co ions during the reaction.[32] $K[(H_2O)_4(3\text{-Hpic})_2\text{-}Nd][(H_2O)_5(3\text{-Hpic})_2Nd][PW_{10}Ti_2O_{40}]\cdot12H_2O$ shows both good catalytic activity and stability after three reuse cycles, with only a slight decrease in the yield from 99.2% to 97.1%.[33] However, POM-based SACs may not be available in strong acids or bases, limited by unstable POM supports. Compared with isolated POM SACs, POM assemblies demonstrate significantly improved stability and reusability during catalytic reactions, as a result of the relatively stable connections between cluster units. Comparable or even higher catalytic activities can be obtained in POM-assembly SACs with ultrathin or single-cluster constructions, owing to the fully exposed active centers and electron transfer between clusters. Nevertheless, the morphologies of POM-assembly SACs are usually unstable at high temperatures (>500 K) due to the organic counterions with poor thermal stability. Additional supports, such as carbon and metal oxides, can be introduced to overcome this issue, where supported POM SACs with thermal and liquid-phase stability can be obtained, but they show relatively poor dispersity compared with pure POM entities.

Xun Wang received his PhD degree from the Department of Chemistry, Tsinghua University, in 2004. He then joined the faculty of the Department of Chemistry, Tsinghua University, in 2004, and was promoted to full professor in 2007. His research interests include the synthesis and applications of ultrathin nanocrystals and cluster-based nanomaterials.

This journal is © The Royal Society of Chemistry 2022

J. Mater. Chem. A, 2022, **10**, 5758–5770 | **5759**

There may also be electron transfer between the metal atoms and POM supports, as revealed by a series of theoretical studies,[34,35] resulting in an interactive electronic structure made of single-atom sites and POM clusters. POM-based SACs with different types of POM support exhibit different catalytic activities, deriving from differences in orbital energies.[36] For a Ru^{III}-substituted phosphotungstic cluster, the HOMO energy of the Keggin structure is higher than that of the Wells–Dawson counterpart, leading to the Wells–Dawson structure showing a lower oxidation potential and higher activity for catalytic water oxidation in comparison to the Keggin-based SAC. The effect of the POM type on the oxidative dehydrogenation of iso-butyraldehyde has also been investigated.[37] Nb- and Ta-substituted POM clusters are able to convert isobutyraldehyde to methyl-isopropanol *via* oxidative dehydrogenation with lattice oxygen. Excellent catalytic activities are generated from the decrease of the LUMO energy caused by the introduction of Nb/Ta with lower electronegativity. In this structure, the LUMO of the POM cluster is mixed from d orbitals on the metal center of the frame and 2p orbitals on the neighboring bridged oxygen, while the HOMO is mainly composed of 2p orbitals from bridging oxygen. Therefore, Nb- and Ta-substitution will only affect the LUMO state of the POM but not the HOMO. The lower LUMO energy results in a smaller HOMO–LUMO energy gap and higher reduction potential, resulting in an enhancement of the catalytic activity. According to the NDR (negative differential resistance) peak voltage, Wells–Dawson-type POM-SACs are always superior to Keggin ones in terms of catalytic activity,

regardless of the substituted metal species. The POM structure can also exert a significant impact on the properties of POM SSCs, as revealed by Yadollahi *et al.*[38,39] $[M_4(PW_9O_{34})_2]^{m-}$ and $[M_4(P_2W_{15}O_{56})_2]^{n-}$ both display high activities for the catalytic oxidation of benzyl alcohol and cycloalkenes, where the catalytic efficiency of Keggin-type $[M_4(PW_9O_{34})_2]^{m-}$ is generally higher than that of Wells–Dawson-type $[M_4(P_2W_{15}O_{56})_2]^{n-}$. Among the available examples, Zn-based SSCs (both Dawson and Keggin) give the best performances for both reactions, with conversions higher than 99% for benzyl alcohol oxidation. Fe-substituted SSCs also show high activity in the catalytic oxidation of cycloalkenes.

3. Isolated clusters as SACs

Via anchoring metal atoms/ions on POM clusters, covalently or non-covalently, the entity of the metal-containing POM cluster can be regarded as a SAC, where the POM group serves as the support. In this section, experimental and theoretical progress relating to individual-cluster SACs is introduced, including POM cluster single-atom catalysts with single metal active sites and single-site catalysts with multiple metal active sites. Various catalytic reactions have been studied with the different types of POM-based SACs, as summarized in Table 1. Keggin- and Wells–Dawson-type clusters are covered in the relevant studies, and the POM clusters are named based on their metal core, where P_2W_{18}/P_2Mo_{18} indicates $[P_2W_{18}O_{62}]^{6-}/[P_2Mo_{18}O_{62}]^{6-}$ and PW_{12}/PMo_{12} stands for $[PW_{12}O_{40}]^{3-}/[PMo_{12}O_{40}]^{3-}$.

Table 1 Reaction types and catalytic performances of POM-based single atom catalysts

Catalyst	Reaction type	Catalytic reaction	Remark	Ref.
$[Ru^{III}(H_2O)SiW_{11}O_{39}]$	Liquid-phase catalysis	Oxidation of styrene	98% (conversion)	40
$[Ru^{III}(H_2O)GeW_{11}O_{39}]$	Photocatalysis	Water oxidation	58.8 h^{-1} (TOF)	41
$[Co(H_2O)_2(SiW_{10}O_{35})_2]$	Photocatalysis	Water oxidation	50 h^{-1} (TOF)	43
$H_7NbP_2W_{17}O_{62}$	Liquid-phase catalysis	Oxidative dehydrogenation of isobutyraldehyde	20% (conversion)	39
$[P_2W_{17}O_{61}\{SnCH_2CH_2C(=O)\}]$	Liquid-phase catalysis	Stereoselective Diels–Alder reaction	100% (conversion)	34
$[(H_2O)_4(3-Hpic)_2Ln][(H_2O)_5(3-Hpic)_2Ln][PW_{10}Ti_2O_{40}]$	Liquid-phase catalysis	Aldehyde cyanosilylation	90% (conversion)	35
$[Ru_4(\mu-O)_4(\mu-OH)_2(H_2O)_4(\gamma-SiW_{10}O_{36})_2]$	Photocatalysis	Water oxidation	>450 h^{-1} (TOF)	49
$[Co_4(H_2O)_2(PW_9O_{34})_2]$	Photocatalysis	Water oxidation	>714 h^{-1} (TOF)	42
$[\{Co_4(OH)_3(PO_4)\}_4(GeW_9O_{34})_4]$	Photocatalysis	Water oxidation	25.8 h^{-1} (TOF)	43
$[Ni_{25}(H_2O)_2(OH)_{18}(CO_3)_2(PO_4)_6(SiW_9O_{34})_6]$	Photocatalysis	Water oxidation	756 h^{-1} (TOF)	44
$[P_2W_{17}O_{61}\{O(SiC_{36}H_{23}N_3O_2Ir)_2\}]$	Photocatalysis	Water-based hydrogen production	0.25 h^{-1} (TOF)	51
$[Mn_4(H_2O)_2(VW_9O_{34})_2]$	Photocatalysis	Water-based hydrogen production	7.64 h^{-1} (TOF)	52
$Na_2K_4[Ni_4(H_2O)_2(PW_9O_{34})_2]$	Photocatalysis	Water-based hydrogen production	116 h^{-1} (TOF)	45
$\{Ni_{14}SiW_9\}$	Photocatalysis	Water-based hydrogen production	97.2 h^{-1} (TOF)	53
$[(Ce(dmso)_3)_2V^{IV}V^V_{11}O_{33}Cl]$	Photocatalysis	Oxidation of indigo	4.80 h^{-1} (TOF)	55
$H_5PV_2Mo_{10}O_{40}$	Liquid-phase catalysis	Oxidation of anthracene	50% (conversion)	57
$H_5PV_2Mo_{10}O_{40}$	Liquid-phase catalysis	Oxidation of dibenzoquinone	~100% (conversion)	54
$[Zn_4(PW_9O_{34})_2]$	Liquid-phase catalysis	Oxidation of alcohols	100% (conversion)	38
$[Zn_4(PW_9O_{34})_2]$	Liquid-phase catalysis	Oxidation of alkenes	99% (conversion)	39

5760 | *J. Mater. Chem. A*, 2022, **10**, 5758–5770

This journal is © The Royal Society of Chemistry 2022
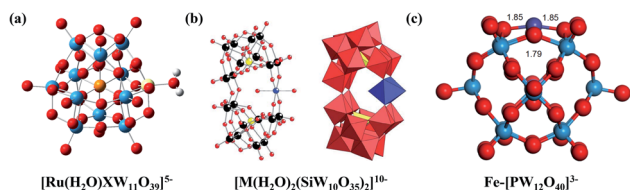
Fig. 1 POM cluster single-atom catalysts. (a) A $[Ru^{III}(H_2O)XW_{11}O_{39}]^{5-}$ cluster; Ru: yellow, W: blue, O: red, H: light gray, Si/Ge: orange; reproduced with permission from ref. 41; copyright: 2011, American Chemical Society. (b) Ball-and-stick (left) and polyhedral (right) representations of $[M(H_2O)_2(c\text{-}SiW_{10}O_{35})_2]^{10-}$ (M = Mn^{II}, Co^{II}, Ni^{II}); W: black, O: red, Si: yellow, Mn/Co/Ni: blue; reproduced with permission from ref. 42; copyright: 2006, Royal Society of Chemistry. (c) The optimized geometry of an Fe-embedded $[PW_{12}O_{40}]^{3-}$ cluster; Fe: purple, W: blue, O: red; reproduced with permission from ref. 34; copyright: 2020, Springer Nature.

3.1 POM cluster single-atom catalyst

Before the proposal of "single-atom catalysts", single-atom substituted POM clusters had already been prepared and applied in the catalytic field. In 1990, Neumann and co-workers reported the synthesis of the Ru-substituted Keggin-type POM $[(C_6H_{13})_4N]_5[Ru^{III}(H_2O)SiW_{11}O_{39}]$,[40] which showed good activity for the catalytic oxidation of styrene. Using $NaIO_4$ as the oxidant, a high yield of 98% can be obtained, with benzaldehyde as the only product. A series of characterization tests was used to investigate atomically dispersed Ru^{3+} on the silicotungstic acid cluster support. In 2011, Fukuzumi *et al.* reported the preparation of $[Ru^{III}(H_2O)SiW_{11}O_{39}]$ and $[Ru^{III}(H_2O)GeW_{11}O_{39}]$ (Fig. 1a), which were then applied for photocatalytic water oxidation.[41] The Ru(v)–oxo complex was confirmed to be the active intermediate, indicating the single-atom active site of Ru during the reaction. Compared with the {$RuSiW_{11}$} cluster, the {$RuGeW_{11}$} complex exhibits higher catalytic activity, which is caused by the electron-withdrawing effects of Ge^{IV}. Other transition-metal-based POM clusters have also been studied, where the lower cost and higher earth abundances may provide better application potential. The Co-substituted Keggin-type

cluster $K_{10}[Co(H_2O)_2(SiW_{10}O_{35})_2]$ (Fig. 1b), first investigated by Kortz and Nadjo,[42] was employed for photocatalytic water oxidation,[32] demonstrating good catalytic activity with a high turnover frequency (TOF, 3.2 s^{-1}) and high quantum yield (27%).

POM clusters can also serve as homogeneous SACs for catalytic reactions in organic systems through a simple encapsulation process involving surface ligands. In 2015, Thorimbert and co-workers reported a stereoselective Diels–Alder reaction catalyzed by chiral hybrid Sn–POM–imidazolidinone clusters.[43] The long-chain nitrogen-containing ligand on the Sn atom forms a chiral ring structure *via* electrostatic interactions and hydrogen bonding between ligands and POM surface atoms. The chiral POM-ligand assembly connected by hydrogen bonding leads to an enantioselective step during the reaction (the mechanism is shown in Fig. 2a). Competitive ion pairing between the positive iminium side chain and either the anionic POM surface or the co-catalyst anion is characterized to be essential, determining the reaction rate and enantioselectivity. When 4-nitrophenylacrylaldehyde is used as the substrate, an overall yield of 100% for the cycloadduct in an 84 : 16 *exo*/*endo* ratio is achieved, with enantioselectivities of 86% and 78%, respectively. A series of Ti- and Ln-containing Keggin-type clusters has also been reported by Zhang *et al.*[33] with different supramolecular constructions of one-dimensional chains and two-dimensional frameworks. Compared with single Ti- or Ln-substitution, the co-substituted cluster displays higher catalytic activity during aldehyde cyanosilylation, which is due to synergy between the Ti-substituted POM and Ln^{3+}. Yields of above 90% are obtained with the substrates of 2-hydroxybenzaldehyde, 4-methylbenzaldehyde, and 4-fluorobenzaldehyde.

Theoretical studies have also been performed on Keggin-type cluster SACs, including potential applications in catalysis and electrocatalysis. In 2017, Su *et al.* performed a DFT study of a supported M_1/PW_{12} cluster (M = Cu, Zn, Ag, Au) for olefin epoxidation (the mechanism is shown in Fig. 2b).[44] The metal active sites located at the fourfold anchoring sites on the POM
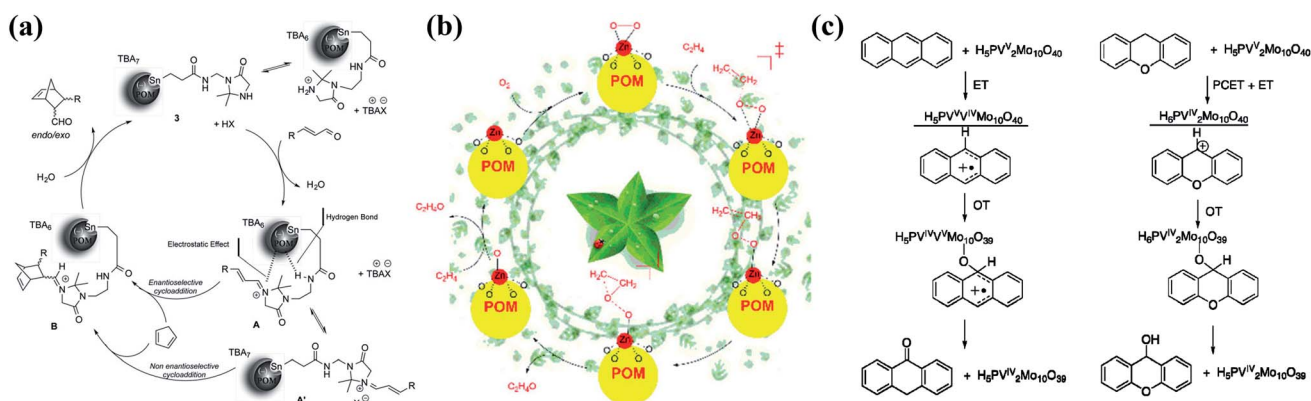

Fig. 2 Catalytic mechanisms for POM-based SACs. (a) The origin of enantioselectivity in the Diels–Alder reaction catalyzed by Sn$_1$/POM; reproduced with permission from ref. 43; copyright: 2015, American Chemical Society. (b) Ethylene epoxidation catalyzed by Zn$_1$/PW$_{12}$; reproduced with permission from ref. 44; copyright: 2017, Wiley-VCH. (c) The catalytic oxidation of anthracene (left) and xanthene (right) *via* an ET–OT mechanism using a $H_5PV_2Mo_{10}O_{40}$ cluster; reproduced with permission from ref. 62; copyright: 2010, American Chemical Society.

This journal is © The Royal Society of Chemistry 2022

J. Mater. Chem. A, 2022, **10**, 5758–5770 | **5761**

surface give the most stable species. Meanwhile, DFT-derived IR spectroscopy indicates the splitting of the four characteristic peaks of the POM into six, which may serve as a feasible way to identify the existence of single metal atom sites on the POM cluster. Among the supported SACs, Cu_1/PW_{12} and Zn_1/PW_{12} display high thermal stabilities, and the Zn/PW_{12} cluster presents the highest activity for the activation of oxygen molecules, which is due to the absorption of oxygen on Zn sites to form a $[POM^{4-}\cdot Zn^{2+}O_2^{-\cdot}]^{3-}$ configuration with the lowest absorption energy. In 2020, another first-principles study on PW_{12}-supported SACs (Fig. 1c) for catalytic ethylene epoxidation was reported by Li et al.[34] The DFT calculation results demonstrate the lower absorption energy of O_2 on the $Fe_1–PW_{12}$ cluster compared with ethylene (Fig. 3a), by which $Fe_1–PW_{12}$ may exhibit higher catalytic activity. According to Bader charge analysis, the Fe atoms embedded on PW_{12} clusters are positively charged, with an atomic charge of about $+1.61|e|$. Electron transfer from the Fe atom to the POM cluster is crucial for the stabilization of Fe single atoms, due to both ionic and covalent interactions. Also, the positive Bader charge indicates the oxidized Fe species form, which may stimulate the catalytic activity of ethylene oxidation due to the high chemical potential and high oxidation state. Owing to the strong spin polarization and magnetism of Fe atoms, the spin density is mainly distributed on Fe atoms. Such a large spin density population at the Fe site may be one of the key factors for the activation of O_2 molecules, because the free electrons on Fe can more easily

coordinate with and activate O_2. The mechanism of the catalytic reaction can be divided into three steps (Fig. 3b): (1) the absorption of O_2 on $Fe_1–PW_{12}$ along with an electron transfer process; (2) attack by the first ethylene molecule of the O_2 molecule absorbed on $Fe_1–PW_{12}$, followed by the formation of ethylene oxide; and (3) a reaction between the second ethylene molecule and the remaining O atom on $Fe_1–PW_{12}$ to form the final product. Moreover, the energy barrier of each step during the reaction is less than 1 eV, which is much lower than the formation of the competing product, acetaldehyde.

The HER (hydrogen evolution reaction), OER (oxygen evolution reaction) and ORR (oxygen reduction reaction) performances of POM SACs were also subsequently investigated, involving PMo_{12}-supported transition metal SACs.[35] Charge density difference analysis shows significant charge transfer between the metal atom and surface oxygen of the POM cluster, and the electron transfer effect decreases with an increase in atomicity. The spin-polarized partial densities of states demonstrate that the d and s orbitals of metal atoms are strongly hybridized, with the 2p orbitals of O atoms at the 4H position close to the Fermi level (EF). In addition, the presence of metal atom d-orbitals near the Fermi level (EF) results in high reactivity, which may trigger the substrates in the catalytic reaction. Calculation data indicate that $Pt_1–$, $Ru_1–$, $V_1–$, and $Ti_1–PMo_{12}$ clusters present the best HER potentials (Fig. 3c), with Gibbs free energies of hydrogen adsorption lower than 0.20 eV, which is close to the ideal zero point. $Co_1–$ and $Pt_1–PMo_{12}$ SACs
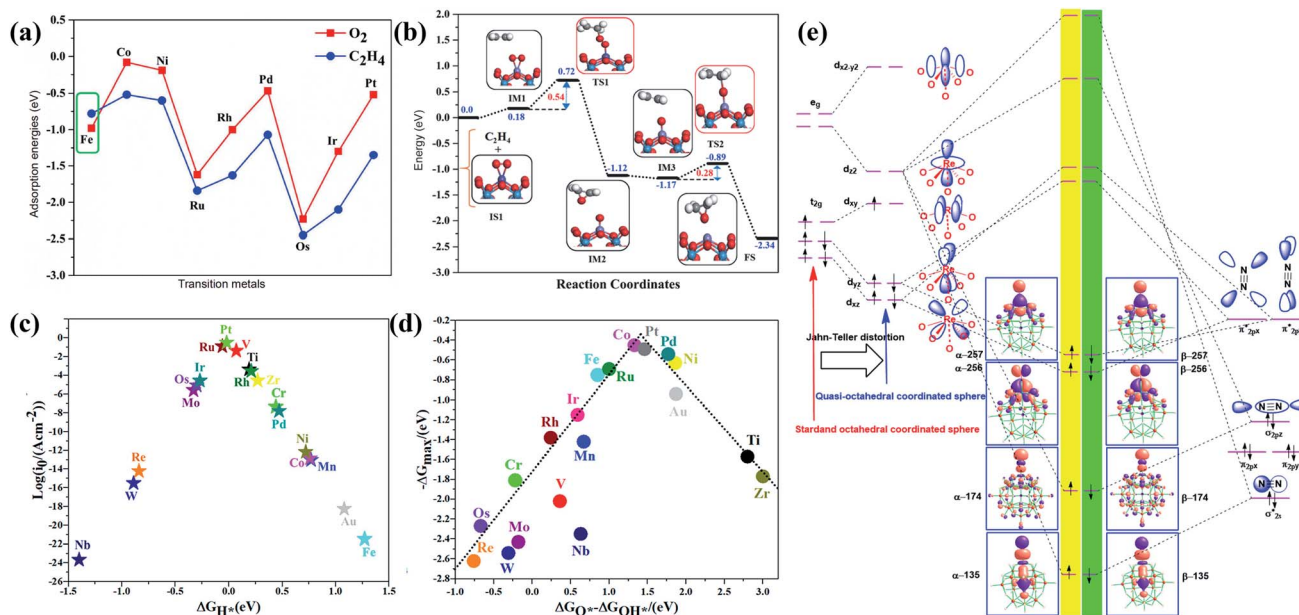

Fig. 3 DFT studies of POM-SACs for ethylene epoxidation (a and b), HER/OER reactions (c and d), and nitrogen reduction (e). (a) The adsorption energies of O_2 (red) and C_2H_4 (blue) on $M_1–[PMo_{12}O_{40}]^{3-}$ clusters (M = Fe, Co, Ni, Ru, Rh, Pd, Os, Ir, and Pt); reproduced with permission from ref. 34; copyright: 2020, American Chemical Society. (b) A schematic energy profile for the epoxidation of ethylene; Fe: blue, P: cyan, O: red, C: gray, H: white; reproduced with permission from ref. 34; copyright: 2020, American Chemical Society. (c) A HER volcano plot of the exchange current (i_0) as a function of the Gibbs free energy of hydrogen adsorption (ΔG_{H*}) over a $M_1–[PMo_{12}O_{40}]^{3-}$ cluster; reproduced with permission from ref. 35; copyright: 2021, American Chemical Society. (d) The OER activity trend of $M_1–[PMo_{12}O_{40}]^{3-}$ showing the maximum potential-limiting (ΔG_{max}) energy vs. the $\Delta G_{O*} − \Delta G_{OH*}$ energy; reproduced with permission from ref. 35; copyright: 2021, American Chemical Society. (e) A schematic representation of Re−N_2 σ donation and π back-donation bonding interactions; reproduced with permission from ref. 46; copyright: 2019, American Chemical Society.

5762 | J. Mater. Chem. A, 2022, 10, 5758–5770

This journal is © The Royal Society of Chemistry 2022

are more suitable for the OER (Fig. 3d), with overpotentials of 0.45 V (Co) and 0.49 V (Pt), which are close to those of MoC_2, IrO_2, and RuO_2. In addition, the overpotential of Fe_1–PMo_{12} for the ORR is calculated to be 0.42 V, which is even lower than that of metallic Pt (0.45 V). POM-based single atom catalysts also exhibit promising potentials in the nitrogen reduction reaction, as revealed by a series of computational studies. The catalytic activities of metal-substituted Keggin POM clusters, $[MPW_{11}O_{39}]^{n-}$, for N_2 activation were investigated via DFT calculations.[46] 21 different transition-metal-substituted POM clusters are involved, and the interactions between the cluster catalysts and N_2 molecules are calculated. Activated Mo, Tc, W, Re, and Os centers show promising application potential for N_2 activation, where Re^{II} is particularly prominent. According to DFT calculations, the catalytic activities of POM SACs derive from interactions between the d_{z^2} orbital of the metal atom and the σ_{2s}^* orbital of bridging nitrogen (Fig. 3e). The metal atom is stabilized in a quasi-octahedral sphere formed from a coordinated N_2 molecule and $[PW_{11}O_{39}]^{7-}$ ligand. Compared with standard octahedrons, the distance between the metal atom center and O atom of the PO_4 tetrahedron is relatively large. The distorted octahedral results in a Jahn–Teller effect in the electronic structure. As a consequence, the energy levels of the d_{z^2}, d_{xz}, and d_{yz} orbitals of the metal–dinitrogen POM complex are reduced, leading to a decrease in the energy gap between the symmetrical orbitals (d_{z^2}, d_{xz}, and d_{yz}) of the metal atoms, significantly promoting atomic orbital interactions between N_2 and the metal center. These results further suggest a distal mechanism for the catalytic nitrogen reduction reaction. Later on, Lin et al. developed a class of stable POM-supported Ru SACs, which can efficiently catalyze the NRR process with overpotentials lower than 0.25 V.[47] Owing to the strong N_2 adsorption abilities of Ru–POM, the competitive HER reaction can also be inhibited.

3.2 POM cluster single-site catalysts

Compared with POM-SACs, the multiple metal centers in POM single-site catalysts (SSCs) are more conducive to multi-electron transfer reactions due to the shorter distances between active sites. For example, {Mn_4Ca} clusters can serve as active centers for photocatalytic water oxidation during photosynthesis, which involves a multi-electron transfer process.[48,49] The sandwich-type POM shells {XW_9O_{34}} are commonly used to wrap the polymetallic center, and the resulting POM SSCs are then applied to photocatalytic hydrolysis.[50–58] Early works on photocatalytic hydrolysis focus on a series of POM clusters with {Ru_4O_4} cores.[54,57] In 2008, Hill and Bonchio obtained $[Ru_4(\mu$-$O)_4(\mu$-$OH)_2(H_2O)_4(\gamma$-$SiW_{10}O_{36})_2]$ SSCs (Fig. 4a) with different counter ions for photocatalytic water oxidation, using $Ru(bpy)_2^{3+}$ and Ce^{4+} as oxidants, respectively. It is confirmed that the Ru active sites exist as tetravalent species. Subsequently, the mechanism of electron transfer between the photosensitizer $(Ru(bpy)_2^{3+})$ and the sacrificial electron acceptor $(S_2O_8^{2-})$ were examined based on transition electron density model theory and time-varying density functional theory.[56] Afterwards, Musaev et al. studied the possible
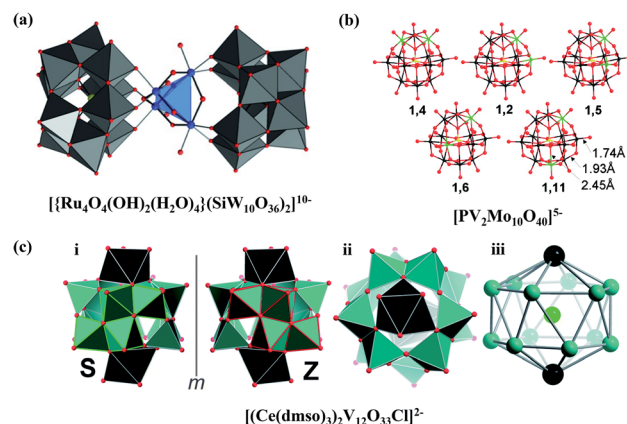

Fig. 4 POM cluster single-site catalysts. (a) A $[Ru_4(\mu$-$O)_4(\mu$-$OH)_2(H_2O)_4(\gamma$-$SiW_{10}O_{36})_2]^{10-}$ cluster, highlighting the central {Ru_4(m-$O)_4$(m-$OH)_2(H_2O)_4$}$^{6+}$ core; Ru: blue, O: red, W: gray, Si: yellow; reproduced with permission from ref. 54; copyright: 2008, Wiley-VCH. (b) Isomers of $H_5[PV_2Mo_{10}O_{40}]$ with key bond lengths; O: red, Mo: black, V: green, P: yellow; reproduced with permission from ref. 62; copyright: 2010, American Chemical Society. (c) (i) The S- and Z-enantiomers of the chiral cerium vanadium oxide cluster $[(Ce(dmso)_3)_2V_{12}O_{33}Cl]^{2-}$. The C_2-symmetric {V_4} building units are highlighted in green (S) and red (Z) outlines. (ii) A top view of the cluster. (iii) The metal-only framework of the cluster. V: teal, Ce: black, Cl: green, O: red. Reproduced with permission from ref. 63; copyright: 2014, Royal Society of Chemistry.

intermediates and the geometric and electronic structures of POM-SSCs in this system,[55] and concluded that the four single-electron oxidation steps involve only the {Ru_4} core orbitals. Due to the worldwide scarcity of Ru, researchers have also paid attention to abundantly available metal active centers, such as cobalt and nickel. In 2010, Hill and co-workers prepared a $[Co_4(H_2O)_2(PW_9O_{34})_2]^{10-}$ cluster with {Co_4} as the active center.[50] For photocatalytic water oxidation, a TOF for O_2 production of ≥5 s^{-1} at pH = 8 was observed. The Co-containing SSC is stable under catalytic turnover conditions, and no cobalt ions or particles were formed in situ. Since then, Wang and co-workers synthesized a series of larger-sized SSCs, such as {Co_{16}}[51] and {Ni_x}[52] (x = 12, 13, 25), which all contain a {M_4O_4} or {M_3O_3} core that is similar to {Mn_4Ca}. Pt-free POM SSCs have also been achieved and employed in photocatalytic water-based hydrogen production. An Ir-based photocatalytic hydrogen production catalyst, a $[P_2W_{17}O_{61}\{O(SiC_{36}H_{23}N_3O_2$-$Ir)_2\}]^{6-}$ cluster, was first obtained by the Proust group in 2012.[59] Since then, $Na_{10}[Mn_4(H_2O)_2(VW_9O_{34})_2]$[60] and $Na_6K_4[Ni_4(H_2$-$O)_2(PW_9O_{34})_2]\cdot32H_2O$[53] SSCs for photocatalytic hydrogen production have been successively synthesized by Hill and co-workers with {M_4O_4} cores and sandwich-type POM shells, similar to photocatalytic water oxidation SSCs. In 2019, other {$Ni_{14}SiW_9$} POM SSCs were realized for similar applications,[61] in which Ni and W active sites jointly participated in the catalytic reaction.

A class of aerobic oxidation reactions can also be realized using POM SSCs, also involving multi-electron transfer processes. The properties of $H_5[PV_2Mo_{10}O_{40}]$ clusters, together with its isomers (Fig. 4b), have been intensively investigated. In

This journal is © The Royal Society of Chemistry 2022

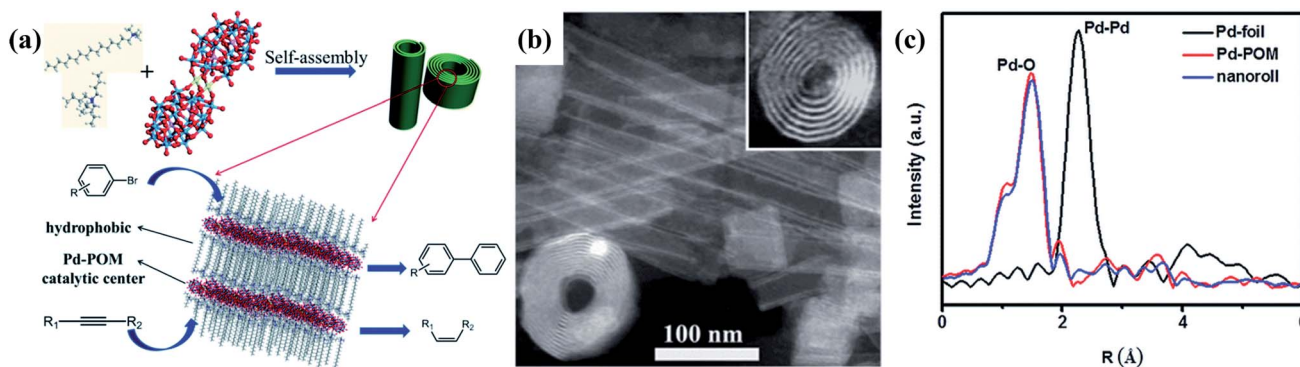J. Mater. Chem. A, 2022, **10**, 5758–5770 | **5763**

Fig. 5 Pd–POM nanoroll assemblies as SACs. (a) A schematic illustration of Pd–POM nanorolls and catalytic reactions; reproduced with permission from ref. 71; copyright: 2016, Royal Society of Chemistry. (b) An STEM image of nanorolls; reproduced with permission from ref. 71; copyright: 2016, Royal Society of Chemistry. (c) The EXAFS fitting curves of Pd foil, Pd–POM, and nanorolls; reproduced with permission from ref. 71; copyright: 2016, Royal Society of Chemistry.

the initial study, vanadium-containing phosphomolybdic acid was employed as the promoter for a Pd-catalyzed oxidation reaction.[45] In 2000, Neumann *et al.* discovered the aerobic liquid-phase oxidation of anthracene and other aromatic substances catalyzed by $H_5PV_2Mo_{10}O_{40}$, which followed a Mars–Van Krevelen type mechanism.[64] Later on, the catalytic oxidation of dibenzoquinone and cyclohexadiene with oxygen was reported by the same group,[62] with a unique ET–OT (electron transfer–oxygen transfer) mechanism (Fig. 2c); electron transfer from the substrate to POM is preferred over oxygen transfer on the POM cluster, which is related to the inertness of V^V toward oxygen transfer. A physical model has been established to show this rationally and to obtain a better understanding of the ET–OT mechanism.[65] They also studied the catalytic activities of five isomers of $H_5PV_2Mo_{10}O_{40}$ *via* theoretical methods. The isomers with V_1 and V_2 close to each other (Fig. 4b, top row) may show different activities in comparison to the isomers with V_1 and V_2 spaced far apart (Fig. 4b, bottom row).[62]

POM-SSCs constructed from a V–O framework show extended light absorption in the visible region, distinct from classic tungstic and molybdate frameworks. A great deal of research into vanadium-based POM SSCs has been carried out by Streb and co-workers, including $\{Bi_4V_{13}\}$,[66] $\{Bi_2V_{12}\}$,[67] $\{Ce_2V_{12}\}$,[63] $\{Ce_2V_{11}\}$,[68] and $\{Mn_4V_4\}$.[68] All these V–POMs exhibit absorption peaks in the visible region. Among them, the $\{Bi_2V_{12}\}$ and $\{Ce_2V_{12}\}$ clusters display interesting chirality (Fig. 4c), always existing as unseparated racemes in crystals. A combined experimental and theoretical study was performed on two halide-templated bismuth vanadium oxide clusters $[X(Bi(dmso)_3)_2V_{12}O_{33}]^-$ ($X = Cl^-$, Br^-). According to DFT calculations, the more efficient triplet excited state formation in the bromide-containing cluster is the decisive step in the photocatalysis of indigo oxidation, which is due to a heavy-atom effect relating to bromide.

4. POM assemblies as SACs

Due to their sub-nanometer size, POM clusters are able to connect *via* non-covalent interactions to form delicate

assemblies with the encapsulation of surface ligands.[69] The introduction of surface ligands greatly promotes the solubility and stability of POM SACs in organic systems, and it can also improve the compatibility between POMs and reactants. The multiple interactions between cluster building blocks and surrounding components, such as electrostatic interactions, hydrogen bonding, coordination bonding, van der Waals forces, and solvophobic interactions, may have a large influence on the electronic structures and properties of clusters, finally causing differences in catalytic performance.[70] Moreover, the insertion of a metal atom results in anisotropic POM building blocks, where specific growth orientations and neoteric morphologies may emerge in the assembly. POM assemblies with ultrathin or single-cluster constructions may present enhanced catalytic activities and stability due to the fully exposed active centers and stable connections between cluster units. The employment of POM-based assemblies as SACs was pioneered by our group in 2015.[71] In the initial work, we developed Pd–POM nanoroll assemblies, using Pd-substituted Dawson-type clusters $[Pd_2(P_2W_{17}O_{61})_2H]$ as building blocks, and the catalyst exhibits excellent catalytic efficiencies toward Suzuki–Miyaura coupling reactions and semi-hydrogenation reactions (Fig. 5a). The self-assembly of Pd–POM clusters is performed *via* the encapsulation of CTAB/TBAB ligands, and resulting nanoroll assemblies with different L/D ratios are shown in Fig. 5b. With the encapsulation of shorter-chain surface ligands, a hollow spindle structure with a length of 500 nm can be obtained in the aqueous phase. EXAFS and XANES tests confirm the existence of atomically dispersed Pd atoms in the structure, where only one peak, at 1.5 Å, from Pd–O contributions is observed (Fig. 5c). As Pd-based SACs, the Pd–POM nanorolls display excellent catalytic activity toward the Suzuki–Niyaura reaction. With a Pd loading amount of 0.13 mol%, a high yield of 96% for 4-acetylbiphenyl can be obtained within 20 min at 303 K, resulting in a TOF of up to 2250 h^{-1}. The excellent catalytic performance can be maintained after four cycles, demonstrating the good catalytic stability of the Pd–POM nanorolls. The catalytic semi-hydrogenation of alkynes was also performed at 298 K, where high yields of 86–91% and high stereoselectivities of $Z/E > 99/1$
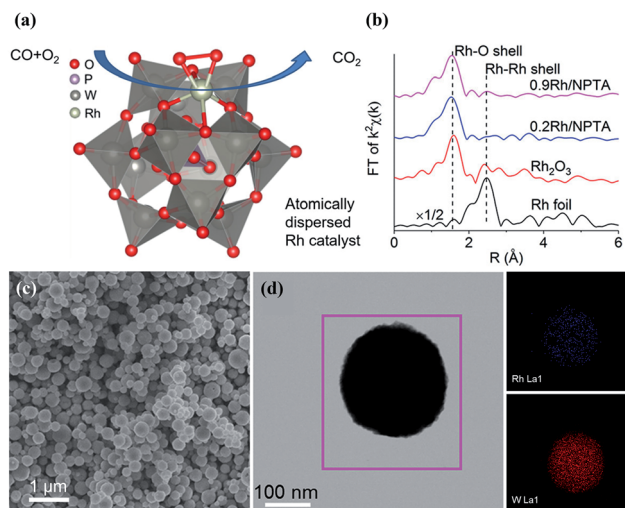
Fig. 6 Atomically dispersed Rh on POM spherical assemblies. (a) The proposed configuration of Rh on the POM cluster; reproduced with permission from ref. 72; copyright: 2017, American Chemical Society. (b) EXAFS spectra of Rh foil, Rh_2O_3, and the Rh−POM assemblies; reproduced with permission from ref. 72; American Chemical Society. (c) An SEM image of Rh−POM spheres; reproduced with permission from ref. 72; copyright: 2017, American Chemical Society. (d) TEM and EDX mapping images of Rh−POM spheres; reproduced with permission from ref. 72; copyright: 2017, American Chemical Society.

for various internal alkynes were achieved within 30 min. In light of this, the Pd–POM nanorolls can be taken as a shape-selective catalyst. During the catalytic reaction, two Pd active centers in the cluster are located on the same side of the reactant, which is beneficial for the hydrogenation of Z-olefins.

Later on, Yan reported Rh–POM porous spherical SACs with Rh loading of up to 0.9 wt% (Fig. 6).[72] POM porous spherical assemblies were prepared through the assembly of $[PW_{12}O_{40}]^{3-}$ and NH_4^+, and the porous structure was constructed *via* the irregular stacking of multiple nanocrystals. *Via* anchoring atomically dispersed Rh on pre-assembled POM spheres, different Rh loading amounts of 0.2–0.9 wt% can be achieved. The EXAFS spectra of Rh–POM assemblies reveal the exclusive existence of Rh as single-atom species (Fig. 6b), which is coordinated to six oxygen atoms through Rh–O bonding. The Rh–POM catalyst is active in CO oxidation, with TOFs between 0.2 and 1.7 s^{-1} from 165 to 195 °C and an apparent activation energy of 127 kJ mol^{-1}. The proposed catalytic cycle consists of alternation between $Rh(CO)_2^{3+}$ species and $Rh(CO)_2^{+}$ species, and the POM support serves as a stabilizer and oxygen transfer mediator to convert CO into CO_2 *via* repeated deoxygenation–oxidation steps. Moreover, the Rh–POM SAC exhibits high thermal stability in CO oxidation after three catalytic cycles (50 to 400 °C), which is superior to isolated POM clusters.

When the size of the assemblies is reduced to a minimum in the form of single cluster constructions, weak interactions between POM clusters and surroundings may have a larger and non-negligible impact on the solution behavior and properties. Thus, single cluster assemblies may show varying assembly behaviors and exceptional properties that are distinct from

conventional nanocrystals and isolated clusters. In 2019, our group reported a general approach for the fabrication of single-cluster nanowires and nanorings, with metal-substituted Dawson POM clusters used as building blocks.[73] The nanowires are able to transform into nanorings upon tuning the pH in the aqueous phase. Among them, the Mn-based nanowires showed excellent catalytic activity during olefin epoxidation. Moreover, 15 kinds of metal-substituted POM clusters can be used to fabricate similar constructions, which are promising candidates to act as SACs.

In a recent study, we successfully prepared a temperature-responsive assembly built from $(CTA)_{3.5}(TBA)_{3.5}[P_2W_{17}MnO_{61}]$ clusters, which can undergo a series of reversible morphology transformations close to room temperature.[74] No temperature-responsive ligands are involved and the stimuli-responsive process is driven by hydrogen bonds. The $P_2W_{17}Mn$ clusters spontaneously arrange into two-dimensional square monolayer superlattices at 25 °C (Fig. 7a and b). At 0 °C, the morphology gradually transforms into single-cluster nanowires (Fig. 7c and d), where a higher aspect ratio is obtained at an even lower temperature (−10 °C). The $P_2W_{17}Mn$ assembly can also serve as a single-atom catalyst, where the Mn active sites are supported by POM anions. Excellent catalytic performance of the $P_2W_{17}Mn$ superlattices towards redox reactions is obtained at 25 °C, with high yields of up to 99% using a series of olefins as substrates. Due to the highly ordered arrangement and POM support as an electron buffer, the $P_2W_{17}Mn$ superlattices show better catalytic efficiency than the well-known Mn porphyrin catalyst Mn(TPP)Cl, with an increase in the TOF of up to 4.16-fold (Fig. 7e). The $P_2W_{17}Mn$ superlattices also exhibit good catalytic stability, with a cyclooctene yield of 92.9% after five cycles. In addition, the 2D superlattice structures exhibit enhanced catalytic performances compared with individual cluster building blocks, which arises from the unique cluster arrangement and coordination of HAc linkers, stabilizing the structure and reducing the activation
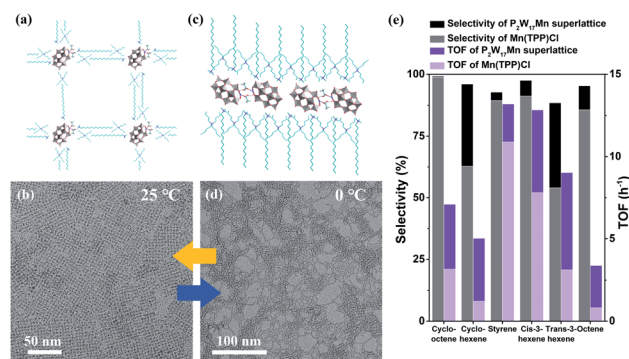

Fig. 7 Mn-Substituted POM cluster assemblies with temperature-responsive properties. (a and b) A molecular model and TEM image of the 2D superlattice structure at 25 °C; reproduced with permission from ref. 74; copyright: 2021, Wiley-VCH. (c and d) A molecular model and TEM image of single-cluster nanowires at 0 °C; reproduced with permission from ref. 74; copyright: 2021, Wiley-VCH. (e) The catalytic performances of $P_2W_{17}Mn$ superlattices and Mn(TPP)Cl in terms of selectivity and TOF; reproduced with permission from ref. 74; copyright: 2021, Wiley-VCH.

This journal is © The Royal Society of Chemistry 2022

J. Mater. Chem. A, 2022, **10**, 5758–5770 | **5765**

energy. Upon the insertion of other metal atoms into POM clusters, single-atom catalysts with different constructions and functions can be realized, which may provide a new pathway for the fabrication of advanced nanomaterials.

5. Supported POM SACs

Treating the POM and metal active center as a whole, the electronic structure of the M–POM entity may be significantly influenced by interactions between M–POM and a support. Promoted electron transfer in a supported SAC may efficiently enhance the catalytic performance. Compared with conventional supported SACs, POM clusters serve as a medium to connect supports and single-atom sites, which can strengthen the bonding with single-atom sites, hence promoting catalytic stability and activity. The introduction of a support provides another dimension for tuning catalytic performance, which provides greater possibilities for the design and application of POM-based SACs. Efforts to obtain supported POM catalysts have already been made, such as POM/MOF and POM/carbon heterogeneous catalysts,[23,75–77] while the loading of single-atom sites on these structures is less common.

5.1 Carbon-supported POM SACs

The oxygen-enriched hydroxyl, ketone, and carboxyl groups on the surface of porous carbon have strong affinity with the surface atoms of POM clusters; therefore, porous carbon can be employed as a feasible support. In 2016, Yan's group developed a strategy for the synthesis of carbon-supported Pt_1/PMo_{12} structures.[78] Keggin-type $H_3PMo_{12}O_{40}$ POM clusters were first attached to the support via wet impregnation, followed by the introduction of $Pt(acac)_2$ (Fig. 8a–c). Among various supports, porous activated carbon shows the best affinity, reaching 100% absorption at room temperature. The POM units with oxygen-rich surfaces have variable coordination modes for Pt

Fig. 8 Carbon-supported Pt_1–PMo_{12} SACs. (a) The most stable configuration of Pt_1 on PMo_{12}/graphene based on DFT calculations; reproduced with permission from ref. 78; copyright: 2016, Wiley-VCH. (b) A TEM image of Pt_1–PMo_{12}/active carbon; reproduced with permission from ref. 78; copyright: 2016, Wiley-VCH. (c) The EXAFS curves of Pt-based and carbon-supported catalysts; reproduced with permission from ref. 78; copyright: 2016, Wiley-VCH. (d) The proposed configurations of Pt_1/POM and the absorption energies of Pt atoms on the supports; reproduced with permission from ref. 79; copyright: 2019, American Chemical Society.

absorption, and the fourfold hollow sites with an absorption energy of −5.72 eV are preferred (Fig. 8a). The carbon-supported Pt_1–PMo_{12} SAC exhibits good performance for the catalytic hydrogenation of nitro and ketone compounds, with 100% selectivity for aniline using nitrobenzene as a reactant. DFT calculations reveal a co-adsorption strategy during the catalytic reaction, where hydrogen adsorption and activation only occur on Pt active sites on POM-SACs.

After that, the influence of the POM support on the behavior of carbon-supported Pt_1–POM SACs was investigated via both experimental testing and DFT calculations (Fig. 8d).[79] According to the DFT calculations, the absorption energy of a Pt single-atom on the POM clusters is the main factor determining the stability of the SAC structure. Keggin-type POM clusters with different compositions, including $H_3PW_{12}O_{40}$ (PTA), $H_3PMo_{12}O_{40}$ (PMA), $H_4SiW_{12}O_{40}$ (STA), and $H_4SiMo_{12}O_{40}$ (SMA), are used as supports, and they can modulate the Pt binding energy by ~2 eV (40%). The catalytic activities of a series of supported SACs toward propene hydrogenation were subsequently studied via experiments and DFT calculations. Due to electron transfer from the Pt atom to the POM cluster, the Pt sites are positively charged, which weakens the absorption of H_2 at Pt active sites. The cationic Pt atoms show large intrinsic energy barriers but small apparent activation energies (~25 kJ mol^{-1}) with different POM supports, owing to endergonic H_2 adsorption and the small adsorption equilibrium constant; this is further confirmed based on experimental tests. In light of this, the enhancements of the catalytic stability and activity of SACs are not contradictory, since the total effective barrier includes several competing factors.

In 2010, Bonchio $et\ al.$ reported the loading of $[Ru_4(\mu\text{-}O)_4(\mu\text{-}OH)_2(H_2O)_4(\gamma\text{-}SiW_{10}O_{36})_2]$ POM SSCs on carbon nanotubes for water oxidation.[57,80] Via grafting positively charged dendrimer chains on carbon nanotube surfaces, POM clusters can be immobilized on the supports through electrostatic interactions. Due to the higher bonding strength of POM SSCs and the promoted electron-transfer process, the catalytic efficiency, operating voltage, current density, and operational stability of the supported POM SSCs for water oxidation were significantly improved. In a recent study, a series of carbon-supported POM SSCs was fabricated via the self-assembly of $[\{Co_4(OH)_3PO_4\}_4(\text{-}SiW_9O_{34})_4]^{32-}$ and ethylenediamine-grafted C_{60} (EDA–C_{60}), followed by an annealing approach to convert the EDA–C_{60} precursor into a carbon support.[81] Fe was then used to replace Co in the $\{Co_4\}$ core, in order to improve the overall catalytic performance. The overpotential of the resulting POM SSC for the OER was measured to be 192 mV (at a current density of 10 mA cm^{-2}), with an almost unchanged OER polarization curve after 6000 CV cycles.

5.2 Metal-oxide-supported POM SACs

Wilkinson catalysts with Rh metal active centers are commonly used as homogeneous catalysts for olefin hydrogenation, but they are easily deactivated and difficult to recover. The anchoring of Rh on a metal oxide support to construct heterogeneous catalysts appears to be an efficient way to solve these
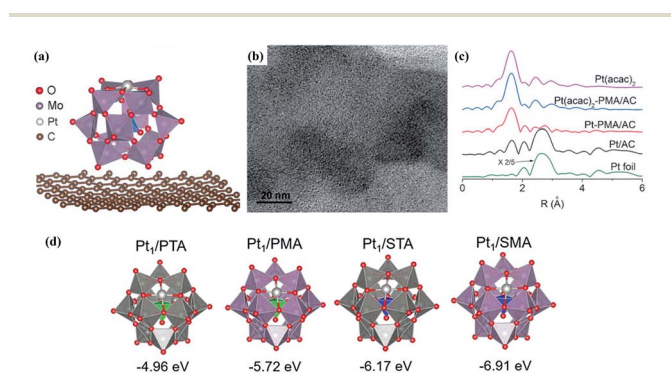
5766 | J. Mater. Chem. A, 2022, **10**, 5758–5770

This journal is © The Royal Society of Chemistry 2022

problems. However, the introduction of a porous support may significantly reduce the overall catalytic activity due to the incomplete exploitation of Rh active sites. In this regard, a novel method has been developed *via* anchoring Rh on POM clusters, which are then loaded on an Al_2O_3 surface. Through ion exchange, metal-oxide-supported Rh(L)–POM SACs with different ligands and POM structures have been prepared.[82–84] Rh active sites bonding to the surface oxygen atoms of POM clusters act as counter ions, which are further covered by other ligands. After modification, the catalytic activities and stabilities of these Rh–POM/Al_2O_3 SACs were greatly improved compared with homogeneous and heterogeneous supported metal (1% Rh/Al_2O_3) catalysts. Due to steric hindrance from the POM support, these catalysts exhibited high stereoselectivity for the *cis*-hydrogenation products.

In addition to Rh SACs, Cu- and Ru-based complexes have also been reported. In 2010, Fraile *et al.* prepared a Cu–PW_{12}/SiO_2 catalyst *via* loading bis(oxazoline)–copper complexes onto a $[PW_{12}O_{40}]^{3-}$ carrier.[85] Compared with the Cu precursor, the supported heterogeneous catalyst exhibits higher activity and stability toward the cyclopropanation reaction, with high yields (of up to 97%) and enantioselectivities in the range of 82–96% for *trans*-cyclopropane over six catalytic cycles. In 2013, a Ru(BINAP)–PW_{12}/Al_2O_3 catalyst was developed following a similar procedure.[86] The Ru-based catalyst displays superior catalytic activity for high-pressure reactions involving β-ketoester hydrogenation, which is due to increased Brønsted acidity contributed by Ru–POM interactions.

5.3 Supported POM SACs based on other materials

Recently, Li and co-workers developed a general strategy for the construction of Pt_1–PMo_{12} SACs supported by a series of frameworks.[87] For the Pt_1–PMo_{12}@MOF SAC, $[PMo_{12}O_{40}]^{3-}$ clusters were first introduced during the crystallization of MIL-101 to form PMo_{12}@MIL-101. Pt(acac)$_2$ was subsequently added to obtain Pt_1–PMo_{12}@MOF *via* an *in situ* reduction process on the POM cluster. As shown in Fig. 9a–c, the Pt single-atom sites are dispersed uniformly throughout the structure, with a loading amount of ~0.24 wt%. Pt_1–PMo_{12}@MIL-101 shows high catalytic efficiency for the diboration of phenylacetylene, with a total yield of 98% and a TOF as high as 1017 h^{-1}, which is six times higher than Pt nanoparticles@MIL-101. DFT calculations demonstrate a pre-concentration effect from the MOF support on the organic substrates and lower energy barriers for the Pt SAC during the reaction compared with Pt nanoparticles, finally leading to the enhancement of the catalytic activity of the Pt_1–PMo_{12}@MIL-101 SAC. Moreover, HKUST-1 and ZIF-67 supports were also used, resulting in similar Pt_1–PMo_{12}@-HKUST-1 and Pt_1–PMo_{12}@ZIF-67 catalysts with Pt loading amounts of 0.41 wt% and 0.13 wt%, respectively.

In the same year, Wang *et al.* reported a carbon–nitrogen (CN) supported Ru_1–WO_x SAC following the strategy shown in Fig. 9d.[88] Here, notched $[PW_{11}O_{39}]^{7-}$ POM clusters were used to fix Ru atoms and prevent Ru from aggregation during pyrolysis. Ru–PW_{11} was then added into a suspension of pre-synthesized anionic polymer coated on SiO_2 for ion exchange. The
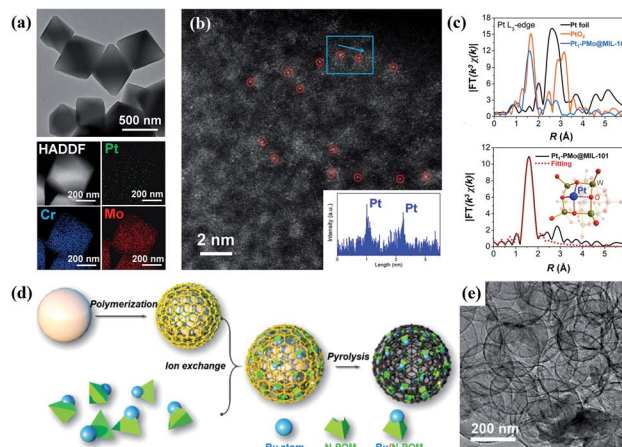

Fig. 9 MOF- and CN-supported POM SACs. (a) A TEM image and the corresponding element mapping results of Pt_1–PMo_{12}@MIL-101; reproduced with permission from ref. 87; copyright: 2021, Springer Nature. (b) An aberration-corrected HAADF-STEM image and corresponding Z-contrast analysis of Pt_1–PMo_{12}@MIL-101; reproduced with permission from ref. 87; copyright: 2021, Springer Nature. (c) EXAFS data and the fitting curves in *R* space for Pt_1–PMo_{12}@MIL-101; reproduced with permission from ref. 87; copyright: 2021, Springer Nature. (d) A schematic illustration of the synthesis of Ru_1–WO_x/CN; reproduced with permission from ref. 88; copyright: 2021, American Chemical Society. (e) A TEM image of the Ru_1–WO_x/CN catalyst; reproduced with permission from ref. 88; copyright: 2021, American Chemical Society.

products were further pyrolyzed and etched with ammonium hydrogen fluoride to remove the SiO_2 template, leading to the formation of the Ru_1–WO_x/CN SAC (Fig. 9e). The Ru_1–WO_x/CN SAC exhibits good catalytic activity for the hydrogenation of levulinic acid to γ-valerolactone (conversion of 99% and selectivity of 100%), with a TOF (1060 h^{-1}) that is 6–7 times higher than those of Ru_1/CN and Ru_1/WO_3 catalysts. The edge oxygen atoms in WO_x are able to link with the carboxyl groups of the substrate *via* hydrogen bonds, resulting in the enhanced absorption of the substrate on the catalyst. DFT calculations indicate a synergistic effect arising from Ru single-atom sites, WO_x clusters, and the CN support, which also contributes to the improvement in catalytic activity. Ag_1–WO_x/CN and Rh_1–WO_x/CN SACs with similar structures can also be fabricated, illustrating the general feasibility of this strategy.

6. Summary and outlook

In this paper, recent progress relating to POM-based SACs is introduced and various applications in the areas of catalytic, electrocatalytic, and photocatalytic reactions are given. Metal-substituted or metal-anchoring POM clusters can serve as SACs or as active sites for the loading of other substrates. Interactions between metal single-atom sites and POM clusters are usually through covalent bonds and coordination bonds, stabilizing the metal sites and allowing electron transfer between metal atoms and POM units. Due to the high stability and electron-rich properties of POM clusters, the introduction of a POM can efficiently tune the electronic properties of metal

This journal is © The Royal Society of Chemistry 2022

J. Mater. Chem. A, 2022, **10**, 5758–5770 | **5767**

active sites and enhance the overall catalytic stability, which may prevent the aggregation and leaching of metal active sites during reactions. Theoretical studies also suggest promoted electron transfer between metal active sites, the POM entity, and any existing support, which appears to be a crucial factor explaining the enhancement in catalytic efficiency. The extraordinary catalytic performances in organic and energy-related fields reveal the promising potential of POM-based SACs as an important member of the single-atom-catalyst family.

Due to oxygenated polyhedron construction, POM clusters can also be regarded as single-site catalysts (Mo/W/V/Nb/Ta as active sites). The overall catalytic activity of a POM cluster is attributed to a synergetic effect between all metal sites in the framework. For POM clusters or POM assemblies with high symmetry, surface charge is distributed uniformly between metal atoms, and no specific active sites are preferred during catalytic reactions. In light of the high stability of POM clusters during redox reactions, the POM entity can be treated as a whole, close to a "superatom". When POM clusters are connected directly to share several atoms, in addition to electrons, the cluster-based assembly can be taken as a supermolecule. Molecular orbital interactions between POM building blocks may lead to changes in energy levels, where exceptional electronic and application properties may emerge. The synthesis of POM-based SACs may focus on POM assemblies with high symmetry, such as 1D nanowires and 2D nanosheets, where POM clusters are closely connected *via* direct bonding. The introduction of secondary components is also encouraged, for example, *via* cluster-nuclei co-assembly,[89] which may greatly extend the functionality of POM-based catalysts. Moreover, future efforts should be made to better understand SACs based on POM clusters, which would also guide the design and synthesis of novel structures with advanced functions. The following points should be noted. (i) Current research into POM-based SACs focuses more on the metal active sites, and the effects of POM supports are partially ignored. Through the modification of POM supports, the catalytic activities of POM SACs can be controlled precisely at the molecular level, which may make the design of SACs with high efficiency more possible. (ii) The molecular models for DFT calculations should be optimized, especially for supported POM SACs, where the POM cluster and support should be taken into account. Future developments in computational chemistry may provide feasible ways to address these issues. (iii) Since POM-based structures are highly sensitive to their surroundings, counter ions (such as quaternary ammonium salts) and interactions between POM clusters may have a non-negligible impact on the structures and properties of POM-based SACs. The relationships between the compositions, structures (morphology), and catalytic properties of SACs should be further investigated, from both experimental and theoretical aspects.

Conflicts of interest

There are no conflicts to declare.

Acknowledgements

Notes and references

1 B. Qiao, A. Wang, X. Yang, L. F. Allard, Z. Jiang, Y. Cui, J. Liu, J. Li and T. Zhang, *Nat. Chem.*, 2011, **3**, 634–641.

2 P. Yin, T. Yao, Y. Wu, L. Zheng, Y. Lin, W. Liu, H. Ju, J. Zhu, X. Hong, Z. Deng, G. Zhou, S. Wei and Y. Li, *Angew. Chem., Int. Ed. Engl.*, 2016, **55**, 10800–10805.

3 X.-F. Yang, A. Wang, B. Qiao, J. Li, J. Liu and T. Zhang, *Acc. Chem. Res.*, 2013, **46**, 1740–1748.

4 L. Liu and A. Corma, *Chem. Rev.*, 2018, **118**, 4981–5079.

5 J. Yang, W. Li, D. Wang and Y. Li, *Small Struct.*, 2020, **2**, 2100007.

6 Z. Chen, J. Liu, M. J. Koh and K. P. Loh, *Adv. Mater.*, 2021, e2103882, DOI: 10.1002/adma.202103882.

7 D. K. Bohme and H. Schwarz, *Angew. Chem., Int. Ed. Engl.*, 2005, **44**, 2336–2354.

8 C. Zhu, S. Fu, Q. Shi, D. Du and Y. Lin, *Angew. Chem., Int. Ed. Engl.*, 2017, **56**, 13944–13960.

9 H. Yan, C. Su, J. He and W. Chen, *J. Mater. Chem. A*, 2018, **6**, 8793–8814.

10 N. Zhang, C. Ye, H. Yan, L. Li, H. He, D. Wang and Y. Li, *Nano Res.*, 2020, **13**, 3165–3182.

11 L. Zeng and C. Xue, *Nano Res.*, 2020, **14**, 934–944.

12 Q. Wang, C. Cai, M. Dai, J. Fu, X. Zhang, H. Li, H. Zhang, K. Chen, Y. Lin, H. Li, J. Hu, M. Miyauchi and M. Liu, *Small Sci.*, 2020, **1**, 2000028.

13 Y. Cui, Z. Cao, Y. Zhang, H. Chen, J. Gu, Z. Du, Y. Shi, B. Li and S. Yang, *Small Sci.*, 2021, **1**, 2100017.

14 R. Lang, X. Du, Y. Huang, X. Jiang, Q. Zhang, Y. Guo, K. Liu, B. Qiao, A. Wang and T. Zhang, *Chem. Rev.*, 2020, **120**, 11986–12043.

15 Z. Liang, C. Qu, D. Xia, R. Zou and Q. Xu, *Angew. Chem., Int. Ed. Engl.*, 2018, **57**, 9604–9633.

16 T. Zhu, Y. Han, S. Liu, B. Yuan, Y. Liu and H. Ma, *Front. Chem.*, 2021, **9**, 717201.

17 A. Han, Z. Zhang, J. Yang, D. Wang and Y. Li, *Small*, 2021, **17**, e2004500.

18 T. Sun, L. Xu, D. Wang and Y. Li, *Nano Res.*, 2019, **12**, 2067–2080.

19 H. Yang, R. Shi, L. Shang and T. Zhang, *Small Struct.*, 2021, **2**, 2100007.

20 C. Busche, L. Vila-Nadal, J. Yan, H. N. Miras, D. L. Long, V. P. Georgiev, A. Asenov, R. H. Pedersen, N. Gadegaard, M. M. Mirza, D. J. Paul, J. M. Poblet and L. Cronin, *Nature*, 2014, **515**, 545–549.

21 J. T. Rhule, C. L. Hill, D. A. Judd and R. F. Schinazi, *Chem. Rev.*, 1998, **98**, 327–358.

22 W. Liu, W. Mu, M. Liu, X. Zhang, H. Cai and Y. Deng, *Nat. Commun.*, 2014, **5**, 3208.

5768 | *J. Mater. Chem. A*, 2022, **10**, 5758–5770

This journal is © The Royal Society of Chemistry 2022

23 Y. Ji, L. Huang, J. Hu, C. Streb and Y.-F. Song, *Energy Environ. Sci.*, 2015, **8**, 776–789.

24 S. S. Wang and G. Y. Yang, *Chem. Rev.*, 2015, **115**, 4893–4962.

25 L. Zong, H. Wu, H. Lin and Y. Chen, *Nano Res.*, 2018, **11**, 4149–4168.

26 L. Lian, H. Zhang, S. An, W. Chen and Y.-F. Song, *Sci. China: Chem.*, 2021, **64**, 1117–1130.

27 D. L. Long, R. Tsunashima and L. Cronin, *Angew. Chem., Int. Ed. Engl.*, 2010, **49**, 1736–1758.

28 H. N. Miras, J. Yan, D. L. Long and L. Cronin, *Chem. Soc. Rev.*, 2012, **41**, 7403–7430.

29 N. V. Izarova, M. T. Pope and U. Kortz, *Angew. Chem., Int. Ed. Engl.*, 2012, **51**, 9492–9510.

30 S. N. Khanna and P. Jena, *Phys. Rev. B: Condens. Matter Mater. Phys.*, 1995, **51**, 13705–13716.

31 A. C. Reber and S. N. Khanna, *Acc. Chem. Res.*, 2017, **50**, 255–263.

32 R. Xiang, Y. Ding and J. Zhao, *Chem. - Asian J.*, 2014, **9**, 3228–3237.

33 H. An, Y. Zhang, Y. Hou, T. Hu, W. Yang, S. Chang and J. Zhang, *Dalton Trans.*, 2018, **47**, 9079–9089.

34 S. H. Talib, X. Yu, Q. Yu, S. Baskaran and J. Li, *Sci. China Mater.*, 2020, **63**, 1003–1014.

35 S. H. Talib, Z. Lu, X. Yu, K. Ahmad, B. Bashir, Z. Yang and J. Li, *ACS Catal.*, 2021, **11**, 8929–8941.

36 K. Nishiki, N. Umehara, Y. Kadota, X. Lopez, J. M. Poblet, C. A. Mezui, A. L. Teillout, I. M. Mbomekalle, P. de Oliveira, M. Miyamoto, T. Sano and M. Sadakane, *Dalton Trans.*, 2016, **45**, 3715–3726.

37 J. H. Choi, D. R. Park, S. Park and I. K. Song, *J. Nanosci. Nanotechnol.*, 2012, **12**, 5864–5869.

38 M. Riahi Farsani, F. Jalilian, B. Yadollahi and H. Amiri Rudbari, *Appl. Organomet. Chem.*, 2015, **29**, 7–11.

39 M. R. Farsani, F. Jalilian, B. Yadollahi and H. A. Rudbari, *Polyhedron*, 2014, **76**, 102–107.

40 R. Neumann and C. Abu-Gnim, *J. Am. Chem. Soc.*, 1990, **112**, 6025–6031.

41 M. Murakami, D. Hong, T. Suenobu, S. Yamaguchi, T. Ogura and S. Fukuzumi, *J. Am. Chem. Soc.*, 2011, **133**, 11605–11613.

42 B. S. Bassil, M. H. Dickman, M. Reicke, U. Kortz, B. Keita and L. Nadjo, *Dalton Trans.*, 2006, 4253–4259, DOI: 10.1039/b606911h.

43 W. J. Xuan, C. Botuha, B. Hasenknopf and S. Thorimbert, *Chemistry*, 2015, **21**, 16512–16516.

44 C. G. Liu, M. X. Jiang and Z. M. Su, *Inorg. Chem.*, 2017, **56**, 10496–10504.

45 M. Lechner, R. Guttel and C. Streb, *Dalton Trans.*, 2016, **45**, 16716–16726.

46 Y. Wang, X. M. Chen, L. L. Zhang and C. G. Liu, *Inorg. Chem.*, 2019, **58**, 7852–7862.

47 L. Lin, L. Gao, K. Xie, R. Jiang and S. Lin, *Phys. Chem. Chem. Phys.*, 2020, **22**, 7234–7240.

48 M. Yagi and M. Kaneko, *Chem. Rev.*, 2001, **101**, 21–36.

49 S. Mukhopadhyay, S. K. Mandal, S. Bhaduri and W. H. Armstrong, *Chem. Rev.*, 2004, **104**, 3981–4026.

50 Q. Yin, J. M. Tan, C. Besson, Y. V. Geletii, D. G. Musaev, A. E. Kuznetsov, Z. Luo, K. I. Hardcastle and C. L. Hill, *Science*, 2010, **328**, 342.

51 X. B. Han, Z. M. Zhang, T. Zhang, Y. G. Li, W. Lin, W. You, Z. M. Su and E. B. Wang, *J. Am. Chem. Soc.*, 2014, **136**, 5359–5366.

52 X. B. Han, Y. G. Li, Z. M. Zhang, H. Q. Tan, Y. Lu and E. B. Wang, *J. Am. Chem. Soc.*, 2015, **137**, 5486–5493.

53 H. Lv, W. Guo, K. Wu, Z. Chen, J. Bacsa, D. G. Musaev, Y. V. Geletii, S. M. Lauinger, T. Lian and C. L. Hill, *J. Am. Chem. Soc.*, 2014, **136**, 14015–14018.

54 Y. V. Geletii, B. Botar, P. Kogerler, D. A. Hillesheim, D. G. Musaev and C. L. Hill, *Angew. Chem., Int. Ed. Engl.*, 2008, **47**, 3896–3899.

55 D. Quiñonero, A. L. Kaledin, A. E. Kuznetsov, Y. V. Geletii, C. Besson, C. L. Hill and D. G. Musaev, *J. Phys. Chem. A*, 2010, **114**, 535–542.

56 A. L. Kaledin, Z. Huang, Y. V. Geletii, T. Lian, C. L. Hill and D. G. Musaev, *J. Phys. Chem. A*, 2010, **114**, 73–80.

57 A. Sartorel, M. Carraro, G. Scorrano, R. D. Zorzi, S. Geremia, N. D. McDaniel, S. Bernhard and M. Bonchio, *J. Am. Chem. Soc.*, 2008, **130**, 5006–5007.

58 C. Besson, Z. Huang, Y. V. Geletii, S. Lense, K. I. Hardcastle, D. G. Musaev, T. Lian, A. Proust and C. L. Hill, *Chem. Commun.*, 2010, **46**, 2784–2786.

59 B. Matt, J. Fize, J. Moussa, H. Amouri, A. Pereira, V. Artero, G. Izzet and A. Proust, *Energy Environ. Sci.*, 2013, **6**, 1504–1508.

60 H. Lv, J. Song, H. Zhu, Y. V. Geletii, J. Bacsa, C. Zhao, T. Lian, D. G. Musaev and C. L. Hill, *J. Catal.*, 2013, **307**, 48–54.

61 G. Paille, A. Boulmier, A. Bensaid, M. H. Ha-Thi, T. T. Tran, T. Pino, J. Marrot, E. Riviere, C. H. Hendon, O. Oms, M. Gomez-Mingot, M. Fontecave, C. Mellot-Draznieks, A. Dolbecq and P. Mialane, *Chem. Commun.*, 2019, **55**, 4166–4169.

62 R. Neumann, *Inorg. Chem.*, 2010, **49**, 3594–3601.

63 A. Seliverstov and C. Streb, *Chem. Commun.*, 2014, **50**, 1827–1829.

64 A. M. Khenkin, L. Weiner, Y. Wang and R. Neumann, *J. Am. Chem. Soc.*, 2001, **123**, 8531–8542.

65 I. A. Weinstock, R. E. Schreiber and R. Neumann, *Chem. Rev.*, 2018, **118**, 2680–2717.

66 J. Tucher, L. C. Nye, I. Ivanovic-Burmazovic, A. Notarnicola and C. Streb, *Chemistry*, 2012, **18**, 10949–10953.

67 J. Tucher, K. Peuntinger, J. T. Margraf, T. Clark, D. M. Guldi and C. Streb, *Chemistry*, 2015, **21**, 8716–8719.

68 B. Schwarz, J. Forster, M. K. Goetz, D. Yücel, C. Berger, T. Jacob and C. Streb, *Angew. Chem., Int. Ed.*, 2016, **55**, 6329–6333.

69 Q. Liu and X. Wang, *Matter*, 2020, **2**, 816–841.

70 Q. Liu and X. Wang, *InfoMat*, 2021, **3**, 854–868.

71 P. He, B. Xu, X. Xu, L. Song and X. Wang, *Chem. Sci.*, 2016, **7**, 1011–1015.

72 B. Zhang, H. Asakura and N. Yan, *Ind. Eng. Chem. Res.*, 2017, **56**, 3578–3587.

73 Q. Liu, P. He, H. Yu, L. Gu, B. Ni, D. Wang and X. Wang, *Sci. Adv.*, 2019, **5**, eaax1081.

This journal is © The Royal Society of Chemistry 2022

J. Mater. Chem. A, 2022, **10**, 5758–5770 | **5769**

74 Q. Liu, H. Yu, Q. Zhang, D. Wang and X. Wang, *Adv. Funct. Mater.*, 2021, **31**, 2103561.

75 P. Mialane, C. Mellot-Draznieks, P. Gairola, M. Duguet, Y. Benseghir, O. Oms and A. Dolbecq, *Chem. Soc. Rev.*, 2021, **50**, 6152–6220.

76 D. Y. Du, J. S. Qin, S. L. Li, Z. M. Su and Y. Q. Lan, *Chem. Soc. Rev.*, 2014, **43**, 4615–4632.

77 D. Wang, L. Liu, J. Jiang, L. Chen and J. Zhao, *Nanoscale*, 2020, **12**, 5705–5718.

78 B. Zhang, H. Asakura, J. Zhang, J. Zhang, S. De and N. Yan, *Angew. Chem., Int. Ed. Engl.*, 2016, **55**, 8319–8323.

79 B. Zhang, G. Sun, S. Ding, H. Asakura, J. Zhang, P. Sautet and N. Yan, *J. Am. Chem. Soc.*, 2019, **141**, 8185–8197.

80 F. M. Toma, A. Sartorel, M. Iurlo, M. Carraro, P. Parisse, C. Maccato, S. Rapino, B. R. Gonzalez, H. Amenitsch, T. Da Ros, L. Casalis, A. Goldoni, M. Marcaccio, G. Scorrano, G. Scoles, F. Paolucci, M. Prato and M. Bonchio, *Nat. Chem.*, 2010, **2**, 826–831.

81 X. B. Han, X. Y. Tang, Y. Lin, E. Gracia-Espino, S. G. Liu, H. W. Liang, G. Z. Hu, X. J. Zhao, H. G. Liao, Y. Z. Tan, T. Wagberg, S. Y. Xie and L. S. Zheng, *J. Am. Chem. Soc.*, 2019, **141**, 232–239.

82 J. A. M. Brandts and P. H. Berben, *Org. Process Res. Dev.*, 2003, **7**, 393–398.

83 S. K. Tanielyan, R. L. Augustine, N. Marin and G. Alvez, *ACS Catal.*, 2011, **1**, 159–169.

84 S. Tanielyan, N. Biunno, R. Bhagat and R. Augustine, *Top. Catal.*, 2014, **57**, 1564–1569.

85 M. Rosario Torviso, M. N. Blanco, C. V. Cáceres, J. M. Fraile and J. A. Mayoral, *J. Catal.*, 2010, **275**, 70–77.

86 S.-H. Ahn, M.-S. Choi, J.-S. Im, R. Sheikh and Y.-H. Park, *J. Mol. Catal. A: Chem.*, 2013, **373**, 55–60.

87 Y. Liu, X. Wu, Z. Li, J. Zhang, S. X. Liu, S. Liu, L. Gu, L. R. Zheng, J. Li, D. Wang and Y. Li, *Nat. Commun.*, 2021, **12**, 4205.

88 Y. Han, J. Dai, R. Xu, W. Ai, L. Zheng, Y. Wang, W. Yan, W. Chen, J. Luo, Q. Liu, D. Wang and Y. Li, *ACS Catal.*, 2021, **11**, 2669–2675.

89 J. Liu, W. Shi, B. Ni, Y. Yang, S. Li, J. Zhuang and X. Wang, *Nat. Chem.*, 2019, **11**, 839–845.